Available online at www.sciencedirect.com
ScienceDirect
Advances in Space Research 38 (2006) 239–252
ADVANCES IN SPACE RESEARCH (a COSPAR publication)
www.elsevier.com/locate/asr

Energetics of the April 2000 magnetic superstorm observed by DMSP

William J. Burke, Cheryl Y. Huang *, Frederick J. Rich

Air Force Research Laboratory, Space Vehicles Directorate, Hanscom Air Force Base, MA, USA

Received 23 December 2004; received in revised form 1 June 2005; accepted 21 July 2005

Abstract

During the late main phase of the April 6, 2000 storm with Dst approaching −300 nT, four Defense Meteorological Satellite Program (DMSP) satellites encountered repeated episodes of intense field-aligned currents whose magnetic perturbations exceeded 1300 nT, corresponding to $|J_{\|}| > 1$ A/m. They had relatively fast rise times (∼5 min) and lasted for ∼20 min. The large magnetic perturbations occurred within the expanded auroral oval at magnetic latitudes below 60°. From Poynting-flux calculations we estimate that during each event several hundred tera-Joules of energy that dissipates in the mid-latitude ionosphere and thermosphere. Ground magnetometers at auroral and middle latitudes detected weak fluctuations that were incommensurate with magnetic perturbations observations at DMSP altitudes. Observed discrepancies between ground and satellite magnetometer measurements suggest that under storm conditions operational models systematically underestimate the level of electromagnetic energy available to the ionosphere–thermosphere. We demonstrate a transmission-line model for M-I coupling that allows calculations of this electromagnetic energy input with no a priori knowledge of ionospheric conductances.
Published by Elsevier Ltd on behalf of COSPAR.

Keywords: Energetics; Magnetic superstorm; DMSP

1. Introduction

It is difficult to grasp that just thirty-five years ago the very existence of field-aligned currents (FACs) was hotly contested (Dessler, 1984; Egeland, 1984). Debate effectively ended when Iijima and Potemra (1976, 1978) showed that not only do FACs exist, their global distributions follow relatively simple patterns, to which they assigned the durable monikers of Region 1 (R1) and Region 2 (R2). R1 currents are located near the poleward boundary of the auroral oval, flowing into the ionosphere on the dawn side of the auroral oval and out on the dusk side. R2 currents are equatorward of R1 and have opposite polarities, flowing into the ionosphere on the dusk side and out on the dawn side.

Huang and Burke (2004) recently reported observations of intense (∼1 A/m) but transient sheets of FACs that couple the central plasma sheet with the auroral ionosphere near maximum epochs of magnetic superstorms. The largest magnetic perturbations are associated with the FACs developed between 55° and 60° magnetic latitude (MLat). Our attention was drawn to these phenomena while comparing ground magnetometer responses to measurements by particle and field sensors on Defense Meteorological Satellite Program (DMSP) satellites during a four-hour period on April 6, 2000. Six empirical aspects of the data appeared to be unusual:

(1) Although four DMSP satellites traversed the FACs at about the same time in the evening and dawn magnetic local-time (MLT) sectors, no commensurate magnetic perturbations were detected at ground stations beneath or conjugate to them. This null result was confirmed in a survey of data from many magnetometer stations at auroral and middle latitudes. Fukushima (1976) predicted this result if driving FACs closed through the ionosphere via meridional Pedersen currents.

* Corresponding author.
E-mail address: Cheryl.Huang@hanscom.af.mil (C.Y. Huang).

0273-1177/$30 Published by Elsevier Ltd on behalf of COSPAR.
doi:10.1016/j.asr.2005.07.085

(2) Pedersen conductances ($\sum_P$) calculated using Ohm's law greatly exceeded estimates estimated from the energy fluxes of precipitating electrons (Robinson et al., 1987). Particle measurements showed that in the plasma-rich environment of this superstorm, electrons carrying the upward FACs showed no sign of field-aligned acceleration and had average energies <500 eV. Electrons with these low energies are stopped at altitudes near 200 km (Rees, 1964) where the ionization they create supports significant Pedersen but little Hall current.
(3) Near the equatorward boundary of the auroral oval in the evening sector, ion number fluxes dominated over those of electrons indicating that precipitating ions were the principal carriers of downward FAC instead of the typical situation with up-going cold electron being the dominant current carriers.
(4) As the evening-sector perturbation decayed, a new upward FAC developed near the equatorward boundary of auroral electron precipitation. Ion fluxes decreased dramatically, suggesting that upward-drifting, low-energy electrons then carried the ~1 A/m downward current.
(5) A significant fraction of ring current energy is transported earthward as Poynting flux that subsequently dissipates in the mid-latitude ionosphere–thermosphere.
(6) Four distinct episodes of intense FACs occurred during the storm's maximum epoch, each following a pseudo-breakup event, apparent in auroral index traces.

Individually and collectively these DMSP observations suggest that under highly stressed conditions, magnetosphere–ionosphere (M-I) coupling is not fully captured in current space-weather models. Richmond and Kamide (1988) outlined an empirical approach to specify FACs and potential distributions that grew into detailed procedures for integrating ground and space data called assimilative mapping of ionospheric electrodynamics (AMIE) (Richmond, 1992). Magnetic perturbations seen by ground stations at high- and mid-latitudes are inverted to specify equivalent ionospheric currents. Translating equivalent currents into realistic electric-field estimates requires knowledge about the distributions of conductance in the modeled ionosphere (Raeder et al., 2001). With varying degrees of success conductances can be estimated from knowledge of solar ultraviolet radiances (Wallis and Budzinski, 1981) and fluxes of precipitating energetic particles (Robinson et al., 1987). However, Kamide et al. (1981) warned that perturbations produced by FACs and poloidal closing currents exactly cancel on the ground (Fukushima, 1976). Under such circumstances AMIE is vulnerable to serious underestimations of FAC intensities and ionospheric electric fields.

M-I coupling involves the exchange of charged particles and electromagnetic energy. The morphologies and origins of energetic particle precipitation into the polar cap and nightside auroral oval are relevant to this report. Winningham and Heikkila (1974) showed that the polar cap is characterized by nearly uniform precipitation of electrons with $E < 100$ eV, called polar rain. Winningham et al. (1975) distinguished between two types of auroral electron precipitation referred to as boundary plasma sheet (BPS) and central plasma sheet (CPS) precipitation. BPS precipitation occurs in the poleward part of the nightside oval and is highly structured in energy-versus-time spectrograms. CPS precipitation occurs in the equatorward part of the oval and varies slowly with latitude. Newell et al. (1996) extended work of Gussenhoven et al. (1983) by sorting ion and electron fluxes by magnetic latitude within the auroral oval and relating empirical boundaries to transitions in the conjugate magnetosphere. Four of the boundaries designated by Newell and coworkers are useful here. From low to high latitude they are: (1) B_1, the equatorward boundary of auroral precipitation which is magnetically conjugate to the instantaneous zero-energy Alfvén boundary; (2) B_{2e} marking entry into the main plasma sheet where average electron energies no longer increase with magnetic latitude; (3) B_{2i}, the ion isotropy boundary which marks the magnetospheric transition between quasi-dipolar and stretched field lines; and (4) B_5, the poleward boundary of the auroral oval. During periods of southward interplanetary magnetic field (IMF) satellites normally encounter polar-rain electron fluxes poleward of B_5.

The Poynting vector $\mathbf{S}(\mathrm{W/m^2}) = \mathbf{E} \times \mathbf{B}/\mu_0$ is the fundamental quantity for representing the energy flux carried by electromagnetic fields (Romer, 1982). The symbols $\mathbf{E}$, $\mathbf{B}$, and μ_0 represent electric fields, magnetic fields, and the permeability of free space, respectively. Kelley et al. (1991) showed how Poynting vectors could be estimated from satellite measurements of ambient electric fields and magnetic perturbations ($\delta\mathbf{B}$) and used as a diagnostic to determine the direction of energy flow within the M-I system. Waters et al. (2004) combined magnetic perturbations measured by the fleet of Iridium satellites joined with electric field measurements from the SuperDARN network to calculate the global Poynting flux during two moderately disturbed periods. Note that to use these techniques great care must be exercised to establish experimental baselines for critical electric and magnetic field measurements (Gary et al., 1994).

Acquiring an experimental ability to measure Poynting fluxes in space spurred an upsurge of theoretical reflection that continues to this day. Thayer and Vickrey (1992) and Thayer et al. (1995) considered implications of Poynting's theorem $\nabla \cdot \mathbf{S} \approx -\mathbf{j} \cdot \mathbf{E}$ for the application of this experimental advance. The symbol $\mathbf{j}$ represents current density. From considerations of the momentum-conservation equation they divided the $\mathbf{j} \cdot \mathbf{E}$ term into two parts, (1) the true Joule heat term is $\mathbf{j} \cdot \mathrm{E}'$, where $\mathbf{E}'$ represents the electric field in the rest frame of the thermospheric neutrals and (2) $\mathbf{u}_n \cdot (\mathbf{j} \times \mathbf{B}_0)$, where $\mathbf{u}_n$ and $\mathbf{B}_0$ represent the neutral wind velocity and the Earth's magnetic field, respectively. If neutral winds act in opposition to local $\mathbf{j} \times \mathbf{B}$ forces the Poynting vector would be directed out away from Earth toward the magnetosphere. Brekke and Kamide (1996) and Song

et al. (2005) developed two- and three-fluid analyses of interactions between electromagnetic fields, neutrals and plasmas. An intriguing feature of on-going theoretical analyses is that in simultaneously solving the momentum and energy equations Vasyliunas and Song (2005) resolved the $\mathbf{j} \cdot \mathbf{E}$ term in the rest frames of the neutrals and the plasma to show that both approaches are valid. This introduces distinctions between energy partitioned to Joule heating of ions, to frictional heating of neutrals, and to driving neutral winds.

This paper concentrates on the energetics of the April 2000 magnetic storm. Because our estimates of energy inputs are based on DMSP measurements we first describe the satellite-orbital characteristics, the scientific payloads, and the spacecraft-centered coordinate system we use for data analysis and presentation. We then summarize two techniques for extracting electromagnetic (EM) coupling parameters from combined particle and field data. One method relies on Ohm's Law and the other on Poynting's theorem (Jackson, 1962). The observations section begins with an overview of the severe magnetic storm of April 6, 2000, including solar wind-IMF inputs and geospace responses represented by variations of the polar-cap potential, geomagnetic indices, and auroral boundaries (Newell et al., 1996). The remainder of the observations section presents the DMSP data required to support empirical result 5 summarized above. The discussion section briefly addresses some implications of DMSP measurements for understanding plasma transport in the magnetosphere and the energy budget of the ionosphere–thermosphere.

2. Instrumentation

DMSP satellites are three-axis stabilized spacecraft that fly in circular, Sun-synchronous, polar (inclination 98.7°) orbits at an altitude of ~840 km. The geographic local times of the orbits are either near the 1800–0600 (F11, F13), or 2100–0900 (F12, 14, 15) local-time meridians. Each satellite carries a suite of sensors to measure (1) fluxes of auroral particles (Special Sensor J4, SSJ4) and (2) densities, temperatures, and drift motions of ionospheric ions and electrons (Special Sensor for Ions Electrons and Scintillations, SSIES). All DMSP satellites designated F12 and higher carry magnetometers (Special Sensor for Magnetic Fields, SSM) to monitor perturbations of the Earth's magnetic field.

Identical SSJ4 sensors are mounted on the top surfaces of DMSP satellites to measure fluxes of down-coming electrons and ions in 19 logarithmically spaced energy steps between 30 and 30 keV (Hardy et al., 1984). Full spectra are compiled every second. Unfortunately, fluxes of ions with energies below 1 keV are unavailable from the F15. SSIES consists of spherical Langmuir probes mounted on 0.8 m booms to measure densities and temperatures of ambient electrons, and three different ion sensors mounted on a conducting plate facing the ram direction. These are: (1) an ion trap to measure the total ion densities; (2) an ion drift meter to measure horizontal (V_H) and vertical (V_V) cross-track components of plasma drift; and (3) retarding potential analyzers (RPA) to measure ion temperature, density and mass and the in-track component of plasma drift $V_\parallel$ (Rich and Hairston, 1994). Because relatively small uncertainties in knowledge about spacecraft potentials often yield large uncertainties in RPA estimates of $V_\parallel$, they are not used in this study. The drift meters measure V_H six times per second, but data are presented as four-second averaged values. SSM sensors are triaxial fluxgate magnetometers that were either mounted on spacecraft surfaces (F12–F14) or a 5 m boom (F15). Magnetic vectors are sampled 12 times per second. One-second average values are calculated as differences between measured and International Geomagnetic Reference Field values of magnetic fields at the spacecraft locations, $\delta\mathbf{B} = \mathbf{B}_{meas} - \mathbf{B}_{IGRF}$. Data are presented as δB_X, δB_Y, δB_Z in the spacecraft-centered coordinate system illustrated in Fig. 1. The X and Y axes point toward spacecraft nadir and along the velocity vector, respectively. The Z axis completes the right-hand system and generally points in the antisunward direction. Fig. 1 shows projections of four DMSP trajectories onto an invariant latitude-versus-MLT grid near 20:20 UT on April 6, 2000. F13 and F14 (F12 and F15) were moving equatorward in the morning (evening) sector above the northern (southern) ionosphere. Nearly simultaneous observations from multiple DMSP satellites help us to understand the electrodynamic of the storm's main phase.

We also make use of interplanetary plasma and magnetic field data from the Advanced Composition Explorer (ACE) satellite in orbit around the first Lagrangian point (L_1), and magnetic indices from the Kyoto World Geomagnetic Data Center. We have extended hemispheric power indices, initially based on electron fluxes measure by NOAA/TIROS satellites (Evans, 1987), to include similar DMSP measurements. The NOAA satellites fly in Sun-synchronous orbits similar to those of DMSP, but their orbital planes are in the afternoon and post-midnight local-time sectors. This extension improves the quality of global

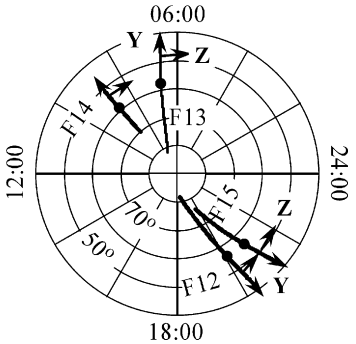

Fig. 1. Spacecraft-centered coordinate system used to analyze SSM data. Trajectories of four DMSP satellites are projected onto an invariant latitude versus magnetic local-time grid. X and Y are directed toward nadir and along the spacecraft velocity vector, respectively. Z generally points toward the antisunward direction. Black circles mark locations on the trajectories where maximum perturbations in δB_Z were detected.

estimates of particle energy deposited at high latitudes. The analysis presented below confirms that electromagnetic energy, while less apparent than that from solar EUV and particle precipitation, is the largest contributor to ionosphere–thermosphere energy budgets during geomagnetic superstorms (Knipp et al., 2004).

3. Data-analysis techniques

Inferences about energy transport under highly stressed conditions derive from the integration of nearly simultaneous measurements from particle and field sensors on four DMSP satellites. Before examining actual DMSP measurements, we briefly describe three complementary techniques used to make quantitative estimates of transferred energy. The first technique is concerned with integrated particle input to the high-latitude ionosphere. The second technique estimates the "Joule heat" input to the ionosphere by solving the current-continuity equation and treating the ionosphere as a resistive load. The third technique uses the transmission-line impedance characteristics to infer EM energy lost in the ionosphere. The latter two techniques utilize electric and magnetic field data streams, presented in spacecraft-centered coordinates, as though DMSP satellites were crossing quasi-infinite FAC sheets at normal incidence. Empirical ways to identify cases where normal-incidence and/or infinite current sheet approximations do not apply are discussed by Burke et al. (1994) and Fung and Hoffman (1992), respectively.

1. The Hemispheric power index (HPI): Evans (1987) developed a climatological model for estimating the total energy per second (power) input to the high-latitude ionosphere due to precipitating electrons. The climatology relies on maps that scale to 10 levels of geomagnetic activity derived from several years of precipitating electron energy fluxes measured by sensors on NOAA/TIROS satellites. The hemispheric power index is defined $\Pi = <\Phi_e> A_i f_{MLT}$, where $<\Phi_e>$ is the average energy flux of precipitating electrons measured as a TIROS satellite crossed the auroral oval, A_i is the area of the auroral oval at level 1 as specified by the intensity of $<\Phi_e>$. The symbol f_{MLT} represents a factor that accounts for variation $<\Phi_e>$ with magnetic local time. One of the authors (FJR) has augmented the NOAA-based values indices to compute Π using DMSP measurements of $<\Phi_e>$ with the specified A_i and f_{MLT} values. We use these computations to compare particle and EM energy inputs to the ionosphere during the April 2000 storm.

2. Ohm's law approach: The equation governing our analysis of combined SSM and SSIES data are Ampere's law

$$j_{\parallel} = (1/\mu_0)[\nabla \times \delta\mathbf{B}]_{\parallel} \tag{1}$$

and current continuity:

$$\partial j_{\parallel}/\partial s = -\nabla_{\perp} \cdot \mathbf{j}_{\perp}. \tag{2}$$

The parameter "s" represents distance along magnetic field lines. In the ionosphere, the current density perpendicular to the Earth's magnetic field $\mathbf{B}_E$ is

$$\mathbf{j}_{\perp} = [\sigma_P \mathbf{E} - \sigma_H(\mathbf{E} \times \mathbf{b})], \tag{3}$$

where σ_P and σ_H are the Pedersen and Hall conductivity, respectively; $\mathbf{b}$ is a unit vector along $\mathbf{B}_E$. Integrating Eq. (2) from the satellite altitude to the bottom of the ionosphere gives

$$j_{\parallel} = \nabla_{\perp} \cdot \mathbf{I}_{\perp} = \nabla_{\perp} \cdot \left[\sum_P \mathbf{E} - \sum_H (\mathbf{E} \times \mathbf{b})\right]. \tag{4}$$

$\sum_P$ and $\sum_H$ represent the Pedersen and Hall conductances, respectively.

Applied to a DMSP satellite crossing an infinite field-aligned current sheet at normal incidence $\nabla_{\perp} \to \partial_Y$, and Ampere's law reduces to $j_{\parallel} = (1/\mu_0)\ [\partial_Y\ \delta B_Z]$. At auroral latitudes FACs into the ionosphere flow nearly in the $+X$ direction. Thus, a positive slope in a δB_Z-versus-time plot indicated current into the ionosphere. Since DMSP moves ~7.35 km/s in the $+Y$ direction, 1 μA/m^2 corresponds to ~9.5 nT/s.

A useful quantity for estimating total currents into or out of the ionosphere is the integrated field-aligned current density (in Amps/m), $J_{\parallel} = \int j_{\parallel}\, dY$. Integration of Eq. (1) along a trajectory segment gives

$$J_{\parallel} = (1/\mu_0)[\Delta \delta B_Z], \tag{5}$$

where the symbol Δ represents the difference between δB_Z values at the applied limits of integration. For reference, $J_{\parallel} = 1$ A/m corresponds to $\Delta \delta B_Z = 1256$ nT.

In a spacecraft-centered coordinate system Eq. (4) becomes $j_{\parallel} = \partial_Y [\sum_P E_Y - \sum_H E_Z]$. For a normal-incidence crossing of a current sheet, E_Z is the electric field component tangential to the sheet direction, which Faraday's law requires to be constant. Combining Ampere's law and current continuity gives

$$\partial_Y \left[\delta B_Z - \mu_0 \left(\sum_P E_Y - \sum_H E_Z\right)\right] = 0. \tag{6}$$

In analyzing SSM and SSIES measurements, we find it useful to identify data segments in which simultaneous variations of δB_Z and E_Y are highly correlated. Eq. (6) shows that during such data acquisitions conductance gradients are weak. Consequently,

$$\sum_P \approx (1/\mu_0)[\Delta \delta B_Z/\Delta E_Y]. \tag{7}$$

Huang and Burke (2004) compared $\sum_P$ estimates using this technique with values calculated using empirical formulas proposed by Robinson et al. (1987), using as inputs simultaneous SSJ4 particle fluxes measurements. Burke et al. (1994) have solved Eq. (6) numerically during a Dynamics Explorer 2 crossing of the auroral oval and successfully predicted the location of an embedded Harang discontinuity.

Frequently DMSP measurements can help identify the charged-particle populations responsible for $j_\parallel$. SSJ4 sensors monitor ion/electron fluxes moving in the $+X$ direction. Differential fluxes measured by SSJ4 may be integrated over energy (30–30 keV) to determine number fluxes $\Phi_{N,\ s}(\phi, \psi)$, in particles/(cm^2 s sr), for both species, s. Here ϕ and ψ represent particles' gyro-phase and pitch angles, respectively. Assuming that both species are gyrotropic,

$$j_\parallel = 2\pi q \int [\Phi_{N,i}(\phi,\alpha) - \Phi_{N,e}(\phi,\alpha)] \cos\psi \sin\psi d\psi \quad (8)$$

here q is the elemental unit of charge 1.62×10^{-19} C. In an upward FAC sheet where both particle distributions are isotropic over the down-coming hemisphere,

$$j_\parallel \approx \pi q[\Phi_{N,i}(\phi,\alpha) - \Phi_{N,e}(\phi,\alpha)]. \quad (9)$$

Eq. (9) is valid to the degree that backscattered are relatively low. In most cases, upward/downward FACs are carried by electrons that move into/out of the ionosphere. During the April 6, 2000 magnetic storm, DMSP detected an unusual case in which an intense downward FAC was carried by precipitating energetic ions (Result 3).

The final physical quantity used as an analysis tool in this paper is the field-aligned Poynting vector $\mathbf{S}_\parallel$ (W/m^2) $= (1/\mu_0)\ [\mathbf{E} \times \delta\mathbf{B}]_\parallel \approx (E_Y \delta B_Z/\mu_0)\ \mathbf{x}$. For reference, E_Y and δB_Z perturbations of 1 mV/m and 1 nT correspond to $S_\parallel \approx 0.8\ \mu$W/m^2. On the time scales of interest, Poynting's theorem relates the divergence in $\mathbf{S}_\parallel$ to the electromagnetic energy dissipated in the ionosphere–thermosphere beneath the spacecraft as

$$\partial S_\parallel/\partial s = -\mathbf{j}_\perp \cdot \mathbf{E} = -\sigma_P E^2. \quad (10)$$

Integrating Eq. (10) from the satellite altitude to the bottom of the ionosphere gives $S_\parallel \approx \sum_P E_Y^2$, the rate at which electromagnetic energy (W/m^2) is dissipated beneath the spacecraft. As pointed out recently by Vasyliunas and Song (2005) the frame of reference dependence of electric fields renders the physical interpretation of Eq. (10) ambiguous. Even under the best of circumstances a determination of $S_\parallel$ requires explicit knowledge of $\sum_P$. As discussed above, the "Joule heat" term in Eq. (10) must be treated with great care.

3. A Transmission-line approach: From a magnetohydrodynamic (MHD) point of view, obliquely propagating Alfvén waves carry FACs (Kan and Sun, 1985). Quasi-steady state currents reflect structures resulting from the superposition of incident (i) and reflected (r) waves. Electric and magnetic field sensors on polar-orbiting satellites detect superposed perturbation fields. In the infinite current sheet approximation, the fields are $E_Y = E_Y^i + E_Y^r$, and $\delta B_Z = \delta B_Z^i + \delta B_Z^r$. The incident and reflected electric fields are related through the relationship $E_Y^r = RE_Y^i$, where $R = (\sum_A - \sum_P)/(\sum_A + \sum_P)$ is the reflection coefficient required for current continuity (Zhu et al., 1993). The Alfvén conductance $\sum_A = 1/(\mu_0 V_{AR})$, where V_{AR} is the Alfvén speed in the reflection layer. Observed separately above the reflection layer, the incident and reflected waves would appear to propagate at the local Alfvén speed $\pm V_{AS}$, i.e., $E_Y^i/\delta B_Z^i = V_{AS} = -E_Y^r/\delta B_Z^r$. Thus, $\delta B_Z^i = -R\delta B_Z^r$.

The ratio of magnetic to electric field variations at the satellite altitude is given by

$$\left[\frac{\delta B_Z}{E_Y}\right]_m = \frac{\delta B_Z^i + \delta B_Z^r}{E_Y^i + E_Y^r} = \frac{1}{(V_{AS})}\frac{1-R}{1+R} = \frac{1}{(V_{AS})}\frac{\sum_P}{\sum_{AR}}. \quad (11)$$

The subscript m signifies measured values of a quantity.

The IGRF model provides excellent estimates of $|\mathbf{B}|$ in the ionosphere. Local plasma densities are measured by SSIES. Across regions of interest, O^+ ions were the dominant species. With this information, we can calculate local values of the Alfvén speed, V_{AS}. Knowing V_{AR} requires unavailable information about the density and mean mass of ions in the reflection layer. However, Eq. (11) allows us to use measured values of V_{AS}, δB_Z, and E_Y to calculate the ratio $\sum_P/\sum_{AR}$ and thereby determine the reflection coefficients R. After presenting stormtime observations, we apply this technique to the analysis of DMSP measurements.

We next consider the physical significance of $S_{\parallel m}$ the "Poynting vector" derived from measured values of δB_Z and E_Y.

$$S_{\parallel m} = \left(\frac{\delta B_{Zm} \times E_{Ym}}{\mu_0}\right) = \left(\frac{\delta B_Z^i(1-R) \times E_Y^i(1+R)}{\mu_0}\right) \quad (12)$$

Defining the incident and reflected Poynting vector as $S_\parallel^i = (\delta B_Z^i \times E_Y^i)/\mu_0$ and $S_\parallel^r = R^2 S_\parallel^i$, we see that $S_{\parallel m}$ is simply the difference between the incoming and out-going electromagnetic energy flux.

$$S_{\parallel m} = S_\parallel^i(1-R^2) = S_\parallel^i - S_\parallel^r. \quad (13)$$

As such it is equivalent to the divergence of the electromagnetic energy flux, which Poynting's theorem indicates is the rate of energy dissipation in the ionosphere–thermosphere beneath the spacecraft. To the degree that $S_{\parallel m}$ can be determined accurately, it provides a measure of energy deposition that requires no a priori knowledge of local Pedersen conductances.

4. Observations

Fig. 2 provides an overview of interplanetary inputs and magnetosphere-ionosphere responses during the last 10 h of April 6, 2000. The top plot shows the interplanetary electric field (IEF) in mV/m. The calculations use a formula for the reconnection electric field derived by Sonnerup (1974); IEF $= VB_T \sin^2(\theta/2)$, where $B_T = (B_Y^2 + B_Z^2)^{1/2}$ and θ is the IMF clock angle in the GSM Y-Z plane. The second plot in Fig. 2 shows the solar wind dynamic pressure P_{SW} in nano-Pascals. The third panel shows polar-cap potentials Φ_{PC} in kilo-Volts measured by four DMSP satellites. Because the satellites cross the high-latitude ionosphere at random attack angles to actual potential

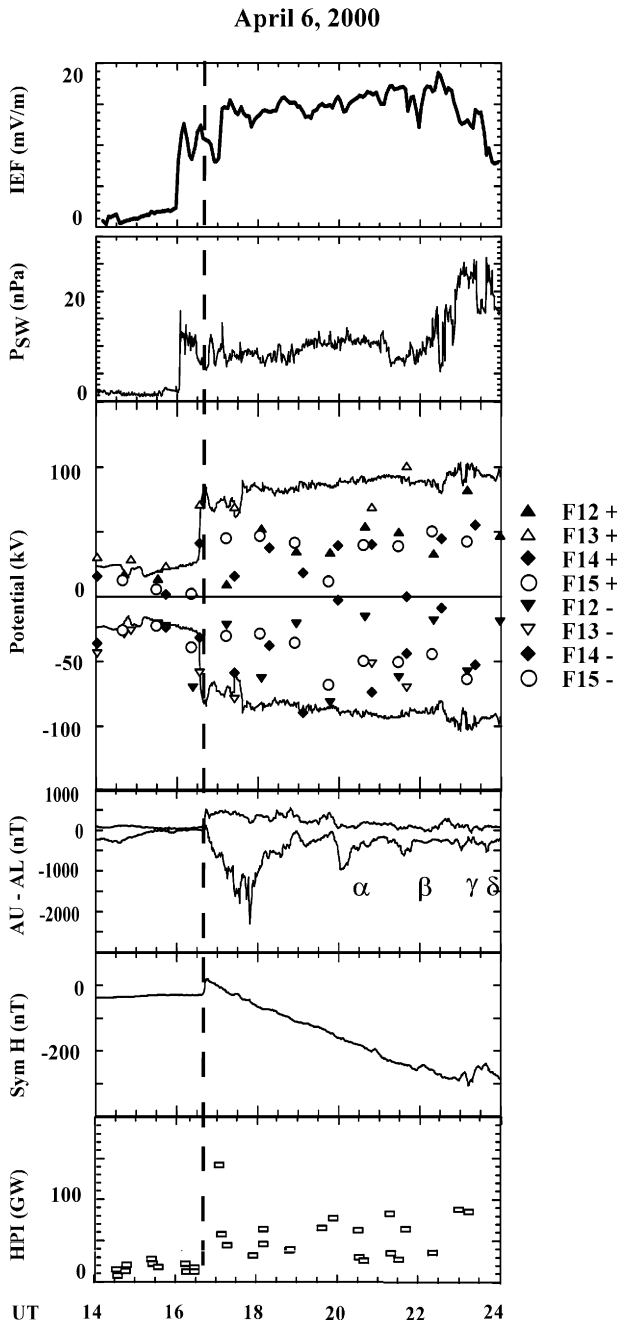

Fig. 2. Interplanetary electric field (top) and dynamic pressure of the solar wind (second) derived from ACE measurements. The third panel compares polar-cap potentials measured by four DMSP satellites with predictions of Hill-Siscoe model. The bottom three panels give the AU – AL, Sym H, and hemispheric power indices.

patterns, DMSP measurements provide lower-bound estimates of the actual Φ_{PC}. Since the orbit of DMSP F13 is closest to the dawn–dusk meridian, its measurements usually provide the best Φ_{PC} estimates. Unfortunately, no F13 data are available between 18:00 and 20:00 UT. The two solid lines indicate values derived from a model of Φ_{PC} suggested by Siscoe et al. (2002) with parameter inputs in forms specified by Ober et al. (2003). The fourth panel shows traces of the auroral electrojet indices AU and AL rather than the frequently presented index AE = AU − AL. This allows us to distinguish between enhancements of DP 1 (substorm wedge) and DP 2 (global circulation) current systems (Nishida, 1968). Similar variations in AU and |AL| signify DP 2 dominance; periods with |AL| ≫AU mark substorm activity. The bottom two panels show the Sym H and hemispheric power indices. Sym H is similar to Dst, but is calculated at a 1-min cadence.

Data show that while the April 6, 2000 magnetic storm was intense, it was also relatively simple in structure. The top plots of Fig. 2 show that an interplanetary disturbance passed the ACE spacecraft at ~16:04 UT when the two parameters increased from about 2 to 12 mV/m and nPa, respectively. When the disturbance reached the vicinity of Earth it caused a sudden storm commencement (SSC) at ~16:43 UT. A steady main phase quickly followed, continuing through the remainder of the day when Sym H reached −300 nT. Sustained recovery began early on April 7. Model values of Φ_{PC}, calculated with a 41-min propagation delay, show a step-function increase near the time of the SSC that closely replicates the increase measured by DMSP F13. Note that calculated Φ_{PC} remained near 170 kV until 22:30 UT when it increased to 200 kV for about an hour. Attention is directed to four brief, excursions of AL, marked by the symbols α, β, γ, and δ, indicating activations of DP 1 currents (substorm/pseudo-breakup events). Four DMSP satellites observed the large-amplitude ($\geqslant 1$ A/m) FAC events reported by Huang and Burke (2004) a few minutes after each of these AL excursions terminated. They all occurred late in the main phase with Sym H < -200 nT. Our attention mostly focuses on electrodynamics associated with event α. A survey of the recent solar maximum period shows that large-amplitude FACs commonly appeared late in the main phase of major storms. DMSP satellites never detect them in a recovery phase. The HPI spiked to 142 GW soon after the SSC then averaged 52.5 ± 21.3 GW for the remainder of the day.

Fig. 3 shows examples of particle and field data acquired in the vicinity of an intense FAC event observed by (a) F15 and (b) F12 in the evening sector, and (c) F13 in the dawn sector, respectively. From top to bottom the five panels for each satellite show: (1) directional energy flux (E-Flux) in eV $cm^{-2}\,s^{-1}\,sr^{-1}$ of down-coming electrons (black) and ions (red); (2) directional number fluxes (N-Flux) of down-coming electrons (black) and ions (red) with energies between 30 and 30 keV, in $cm^{-2}\,s^{-1}\,sr^{-1}$; (3) average energy of precipitating ions (red) and electrons (black), defined as E_{AVE} = E-Flux/N-Flux (calculated this way, E_{AVE} is about twice the mean thermal energy of the species population (Robinson et al., 1987)); (4) the cross-track component of the magnetic field deflection δB_Z in nanotesla; and (5) the in-track component of the electric field E_Y calculated from the observed ion drift and IGRF magnetic field values (Rich and Hairston, 1994). For ease in comparing data we have plotted E_Y on the same scale for all three satellites and inverted the sign of E_Y in plots for F15 and F12. Vertical

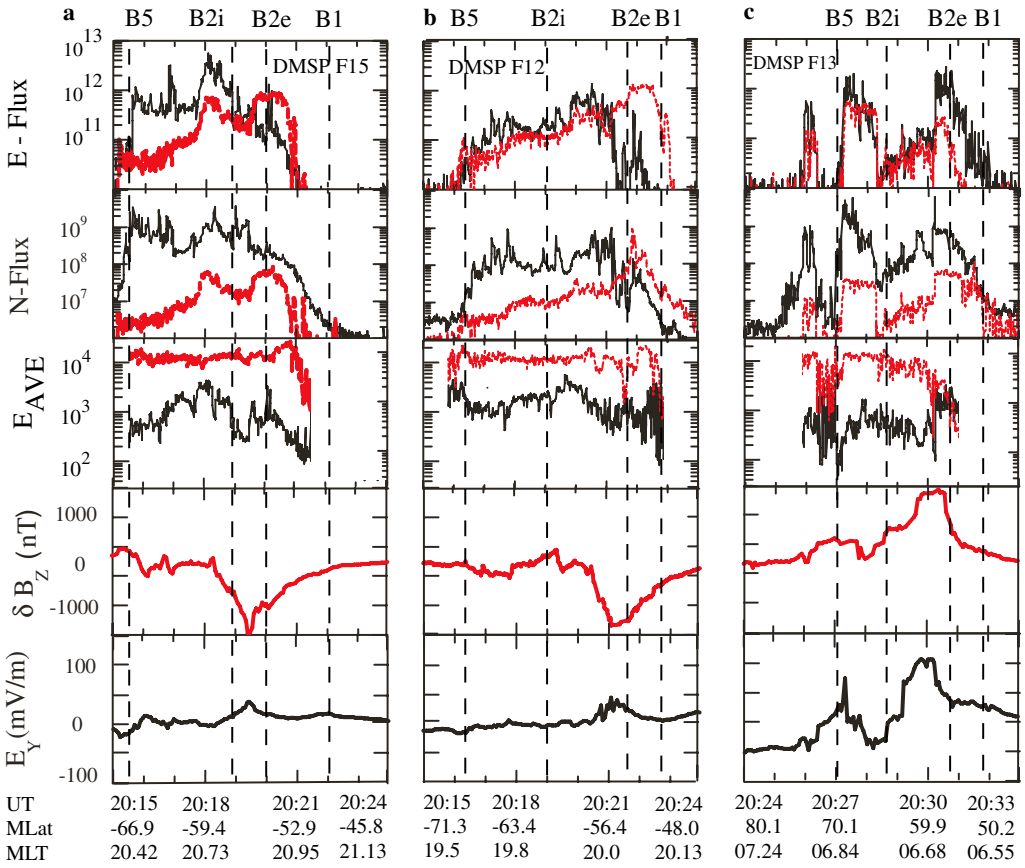

Fig. 3. Particle and field measurements by (a) DMSP F15 and (b) F12 in the evening sector after 20:15 UT, and (c) F13 in the morning sector after 20:24 UT on April 6, 2000. From top to bottom the panels for each satellite show: (1) directional energy flux (E-Flux) in eV $cm^{-2}\,s^{-1}\,sr^{-1}$ of down-coming electrons (upper line) and ions (lower line); (2) directional number fluxes (N-Flux) of down-coming electrons (upper line) and ions (bottom line) with energies between 30 and 30 keV, in $cm^{-2}\,s^{-1}\,sr^{-1}$; (3) average energy of precipitating ions (upper line) and electrons (lower line), defined as E_{AVE} = E-Flux/NFlux; (4) the cross-track component of the magnetic field δB_Z in nanotesla; and (5) the in-track component of the electric field E_Y calculated from the observed ion drifts. For the sake of comparison the polarity of E_Y in plots of F15 and F12 were reversed. Vertical dashed lines indicate times when the satellites crossed B_1, B_{2e}, B_{2i}, and B_5. (For interpretation of the references to color in this figure legend, the reader is referred to the web version of this paper.)

dashed lines indicate times when the DMSP satellites crossed the B_1, B_{2e}, B_{2i}, and B_5 boundaries (Newell et al., 1996). Data are plotted as functions of UT, MLat, and MLT.

Fig. 3a shows that F15 entered the evening sector auroral oval from the southern polar cap (B_5) near 20:15:30 UT. A rapid rise in electron fluxes (panel 2) and a reversal in E_Y (panel 5) mark the transition. Attention is directed to the ~1500 nT decrease in δB_Z detected between 20:18:10 and 20:19:30 UT (panel 4). This nearly uniform decrease in δB_Z in time corresponds to a 2 $\mu A/m^2$ outward FAC, a net electron flux of $\sim 10^9\,cm^{-2}\,s^{-1}$ into the ionosphere. Fig. 3a also shows down-coming electron fluxes $>10^9\,cm^{-2}\,s^{-1}\,sr^{-1}$ in the upward FAC sheet (panel 2). Assuming isotropic fluxes over the down-coming hemisphere, we see that electrons with energies between 30 and 30 keV can account for the observed upward FAC. The E_{AVE} plot (panel 3) indicates that most current-carrying electrons equatorward of B_{2i} had $E < 500$ eV. The largest δB_Z deflection, marking the interface between upward and downward FAC sheets, occurred near −56° MLat between B_{2i} and B_{2e}. A deflection of 1500 nT corresponds to $J_\parallel \approx 1.2$ A/m or ~1.2 MA for every 1000 km extent in longitude (~1 h in LT). Current continuity requires that a height-integrated Pedersen current J_P, equal to $J_\parallel$, flows across the interface between the upward and downward FAC sheets. Near the transition between upward and downward FAC sheets, a maximum electric field of ~40 mV/m was inferred from drift meter measurements and the local IGRF magnetic field. This implies that at the transition $\sum_P = J_P/E_Y \approx 30$ mho. To facilitate direct comparisons between electric fields measured in the evening and dawn MLT sectors, we have plotted $-E_Y$ for F 15 and F12 and $+E_Y$ in the bottom panels of Figs. 3a–c on the same scale. This suppresses information, available in standard ion drift meter displays that indicate a 1 km/s subauroral ionospheric drift event equatorward of B_1. Discernable magnetic deflections due to R2 currents and subauroral electric fields extend equatorward to about −45° MLat.

DMSP F12 crossed the auroral oval near 20 MLT, less than 2 min after F15, where it detected similar δB_Z and E_Y variations. Particle fluxes measured by the SSJ4 sensor on

F12, shown in Fig. 3b, panel 2, yield one more relevant observation that differs significantly from the F15 observations. Data plotted in Fig. 3a, panels 1 and 2, show that on F15 in the downward FAC region, energy fluxes of downcoming ring current ions exceeded those of precipitating electrons. However, the electron number fluxes were always greater than those of ions. DMSP F12 measurements in Fig. 3b, panels 1 and 2 indicate that across the downward current sheet (MLat $> -56°$) ion number fluxes were larger than those of electrons by a factor of two or more. The difference is attributed to intense fluxes of low energy (<1 keV) ions that the SSJ4 sensor on F12 could detect, but the one on F15 could not.

Fig. 4 shows DMSP F12 measurements acquired between 20:20 and 20:23 UT in greater detail. Fig. 4a repeats the δB_Z trace. Fig. 4b shows the difference between electron and ion number fluxes. The vertical dashed line marks the approximate location of the transition from upward to downward FACs. To the left of this line where the δB_Z trace has a negative slope indicating a current out of the ionosphere, the flux of precipitating electrons exceeds that of the ions by $\sim 3 \times 10^8/(\mathrm{cm}^2\,\mathrm{s\,sr})$. Near 20:22 UT the opposite FAC polarity is observed and the precipitating ion flux dominates. Figs. 4c and d show 5-s averaged electron and ion spectra centered near 20:21:00 and 20:21:51 UT in the upward and downward FAC sheets, respectively. In the upward FAC sheet, low-energy (<1 keV) electrons dominate the distribution. The spectrum gives no indication that the current-carrying electrons experienced a field-aligned acceleration. This indicates that the conjugate plasma sheet had a sufficiently high density to provide the required $j_\parallel$ without generating a field-aligned potential drop (Lyons, 1981). In the downward FAC sheet the flux of <1 keV ions almost matches that of the electrons. At energies >2 keV the ion spectrum is relatively flat, indicating the presence of substantial fluxes at energies >30 keV, the upper limit of SSJ4 detection. Since DMSP satellites cannot monitor upward electron or ion fluxes, it is normally reasonable to assume that most of the downward current is carried by upward flowing cold electrons. However, the DMSP F12 data in Figs. 4b and d strongly suggest that the flux of precipitating ions dominated over electron fluxes.

Returning to Fig. 3c, we see that DMSP F13 acquired data near the dawn meridian in the northern ionosphere. Electron fluxes (panel 2) rose above polar-rain levels at ~20:25:50 UT. The polarity of E_Y reversed ~30 s later. F13 entered the main oval (B_5) just before 20:27:00 UT. In the region poleward of B_5, electron and ion fluxes were often near background levels, leading to large, non-geophysical variations in calculated values of E_{AVE}. Since the polar cap is outside the domain of concern for this paper, we do not display E_{AVE} values in this region. A comparison with data in Fig. 3a, panels 1 and 2 indicates that BPS electron precipitation was more structured in the dawn than in the evening sector (Winningham et al., 1975). Particle fluxes observed in the morning sector by F11 and F14 (not shown) were similar to those of F13. Electron energy fluxes >1 erg $\mathrm{cm}^{-2}\,\mathrm{s}^{-1}\,\mathrm{sr}^{-1}$ were observed for more than a minute after 20:27 and 20:30 UT. A pair of intense FAC sheets, with a magnetic deflection >1400 nT (~1.1 A/m), was observed near 20:30 UT (panel 4). A sharp intensification of electron fluxes (panels 1 and 2) marked the transition from downward to upward FAC. In this case, $E_Y \approx 90$ mV/m was inferred from drift meter measurements near the maximum δB_Z. In the region

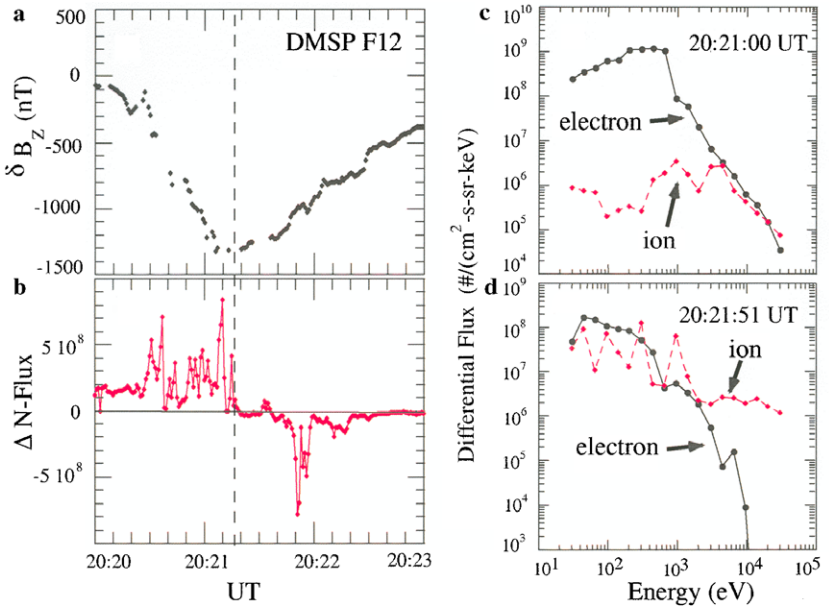

Fig. 4. Characteristics of the FAC sheets crossed by DMSP F12 between 20:20 and 20:23 UT. Panels show (a) variations of δB_Z and (b) differences between electron and ion number fluxes as a function of UT, as well as five-second averaged ion and electron spectra measured by SSJ4 within the (c) upward and (d) downward FAC sheets.

of the downward FAC, low ion fluxes indicate that up-going ionospheric electrons were probably the prime current carriers. Again the maximum deflections in E_Y and δB_Z occurred between B_{2e} and B_{2i}. Finally, we note that in both the morning and evening sectors, the δB_Z traces indicate that Region 2 FACs extended to subauroral latitudes.

The relatively close orbital phasing of DMSP spacecraft on April 6, 2000 facilitated our analysis of data acquired during this magnetic storm. F11, F13, and F14 crossed the high-latitude ionosphere in the same hemisphere within 2 min of each other. The F12 and F15 spacecraft flew over the conjugate polar ionosphere ~10 min earlier than the F11, F13, and F14 auroral passes, but within 1.5 min of each other. Table 1 lists the UT, as well as the magnetic and geographic coordinates at which the DMSP satellites crossed the largest FAC perturbations. Values of the largest amplitude of $|\delta B_Z|$ appears in the eighth column. Maxima for $|E_Y|$ were acquired spatially close to, but not necessarily coincident with, δB_Z extrema. Spatial separations in the extrema of δB_Z and E_Y indicate the presence of latitudinal conductivity gradients near the interface between upward/downward FAC.

Three empirical aspects of data in Table 1 deserve comment. First, δB_Z extrema measured by all of the satellites corresponded to FACs with $J_\parallel > 1$ A/m. Second, all δB_Z extrema were observed equatorward of MLAT = 60°. (MLat, as used herein, is the corrected geomagnetic latitude of the point obtained by tracing the geomagnetic field down to 110 km altitude and then projecting down to the ground. It is very close to but not identical to invariant latitude.) Third, electric fields detected at similar MLTs had comparable values. The latitudinal distributions of E_Y detected by F11 and F13 were nearly identical across the morning auroral oval. Comparing bottom panels of Figs. 3a–c, however, we see that evening-sector values of E_Y were about half their morning side counterparts, indicating about a factor of two higher conductances in the evening auroral ionosphere.

In the remaining analysis of DMSP data we adopt $|\delta B_Z|_{max}$ as our organizing parameter for understanding M-I coupling. This choice is dictated by two considerations. First, Eq. (5) shows that $|\delta B_Z|_{max}$ is directly proportional to $J_\parallel$, the integrated FAC coupling the magnetosphere to the ionosphere. As such it maps to the ionospheric footprint of maximum Pedersen current. Second, during the magnetic-storm's main phase $|\delta B_Z|_{max}$ was observed at relatively low magnetic latitudes that normally map to the inner magnetosphere.

We have derived relationships between δB_Z and E_Y variations required for current continuity in the ionosphere beneath DMSP satellites. In regions of near uniform conductance Eq. (6) reduces to $\sum_P = \Delta\delta B_Z/[\mu_0\ \Delta E_Y]$; in practical units $\sum_P$ (mho) = $\Delta\delta B_Z$ (nT)/[1.256 · Δ E_Y (mV/m)]. This equation assumes that the infinite current sheet approximation is valid. For the events of Fig. 3, simultaneous δB_Z and δB_Y variations were nearly monotonic and highly correlated, indicating that the spacecraft indeed crossed quasi-infinite current sheets at nearly constant attack angles $\alpha = \tan^{-1}(\delta B_Z/\delta B_Y)$. Values of α listed in the last column of Table 2 show that the DMSP satellites crossed FAC sheets at nearly normal incidence. Fung and Hoffman (1992) addressed the general case for identifying where end effects or filamentary structures are important.

Table 2 also summarizes information contained in Fig. 3. Listed data indicate the beginning UT_I and duration Δt of intervals in which δB_Z and E_Y variations were highly correlated, consistent with crossing strips of nearly uniform $\sum_P$. Correlation coefficients within the current sheets were >0.98. Values of $\sum_P$ estimated from δB_Z and E_Y variations within the intense upward and downward FAC sheets are listed in column 8 of Table 2. Except in the downward FAC that F13 sampled estimated values of $\sum_P$ were >25 mho.

Measurements by the SSJ4 sensors allow independent estimates of the ionospheric conductance using empirical formulas suggested by Robinson et al. (1987).

$$\sum_P = [40E_{AVE}\sqrt{(\Phi_E)}]/[16 + E_{AVE}^2] \quad (14)$$

and

$$\sum_H = 0.45\sum_P (E_{AVE})^{0.85}. \quad (15)$$

Table 1
Extrema of δB_Z and E_Y

DMSP	UT	MLAT	MLT	MLONG	GLAT	GLONG	$\lvert\delta B_Z\rvert$ (nT)	$\lvert E_Y\rvert$ (mV/m)
F12	20:21.2	−56.1°	19.9	66°	−55.0°	14.5°	1326	41.5
F13	20:30.3	+59.1°	6.7	225°	+63.1°	159.9°	1424	91.5
F14	20:30.7	+61.2°	8.8	255°	+61.2°	199.8°	1354	82.9
F15	20:19.4	−55.9°	20.9	79°	−52.2°	26.3°	1506	42.5

Table 2
Auroral FAC circuit parameters

DMSP	UT_I	Δt (s)	δB_{ZI} (nT)	δB_{ZF} (nT)	E_{YI} (mV/m)	E_{YF} (mV/m)	$\sum_P$ (mho)	α
F13	20:28:46	64	600	1340	3.0	105.4	5.9	68.3°
F13	20:30:30	21	1370	498	48.5	25.4	30.0	83.9°
F15	20:18:22	64	−218	−1487	0.4	37.4	27.3	84.5°
F15	20:19:30	76	−1469	−496	34.7	9.8	31.1	89.2°

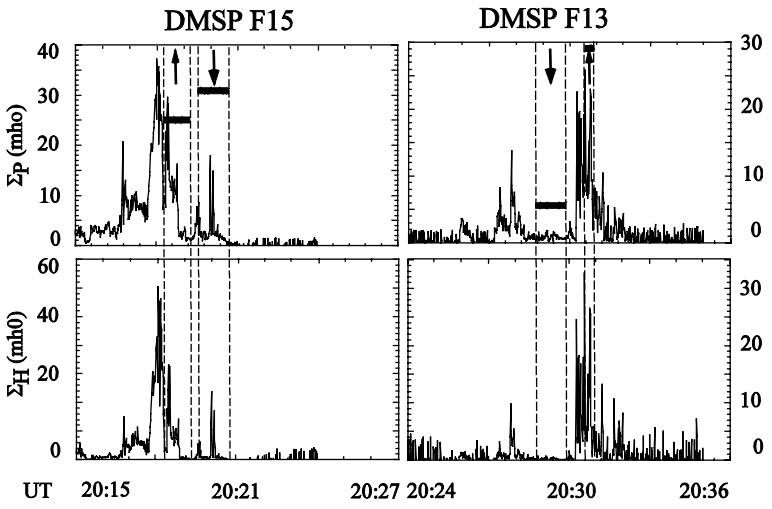

Fig. 5. $\sum_P$ (top) and $\sum_H$ (bottom) estimated from electron fluxes measured by F15 (left) and F13 (right). Horizontal lines indicate $\sum_P$ estimated from δB_Z and E_Y variations.

Here, E_{AVE} represents the average energy of precipitating electrons in keV and Φ_E is the electron energy flux in ergs/(cm^2 s). To help estimate ionospheric conductances we assume that electron distribution functions were isotropic over the down-coming hemisphere. Calculated values of $\sum_P$ (top) and $\sum_H$ (bottom) due to energetic electron precipitation observed by F15 (left) and F13 (right) are plotted as functions of UT in Fig. 5. The vertical dashed lines mark the intervals during which we estimated $\sum_P$ from highly correlated δB_Z and E_Y variations. The downward and upward pointing arrows located between the dashed lines signify the directions of FACs into and out of the ionosphere, respectively. Heavy horizontal bars within the dashed lines indicate calculated values of $\sum_P$ listed in Table 2. When we compare Pedersen conductances estimated using two different techniques, we see that the average values of $\sum_P$ estimated from Eq. (12) were significantly lower than those obtained from Eq. (7). Solar generated conductance is ignored because all observations are made when the ionosphere below 200 km is in darkness. Attention is directed to the upward current sheets where observed variations of δB_Z and E_Y were monotonic (Fig. 5) and highly correlated. Here, Eq. (6) indicates that $\sum_P$ should have been constant. In both instances $\sum_P$ plots in Fig. 5 estimated from electron measurements suggest the presence of gradients.

Except in the region of upward FACs detected by F13, values of $\sum_P$ estimated using the electromagnetic technique are much higher than estimates based on electron fluxes. We suggest three possible reasons for the discrepancy. First, the current-continuity calculations of $\sum_P$ are most valid along trajectory segments where the conductance is nearly constant. $\sum_P$ distributions determined from electron fluxes indicate that this condition was not always met. Second, during the main phase of this storm electron fluxes were outside the limits of validity of the Robinson et al. (1987) formulas. Third, Eq. (6) assumes that the M-I circuit is in steady state. F13 and F14 detected relatively small values of $|\delta B_Z|_{max}$ in the evening auroral oval a few minutes before F12 and F15 observed the newly activated, intense FAC circuit. It takes several Alfvén bounce periods for the M-I circuit to reach equilibrium (Kan and Sun, 1985); thus, we must also consider transmission line effects. We address these three possibilities in turn.

1. Conductance gradients: Variations in energetic electron fluxes measured as DMSP satellites crossed individual FAC sheets show that $\sum_P$ gradients exist on small (~10 km) spatial scale sizes. Indeed, small-scale variations evident in δB_Z and E_Y traces witness similar-scale $\sum_P$ gradients. For two reasons we believe that conductance gradients are not as severe as suggested by estimates presented in Fig. 5. First, in choosing regions to estimate $\sum_P$ from δB_Z and E_Y variations, we required that the correlation between the two data sets exceed 0.98. Second, in the vicinity of δB_Z and E_Y extrema, conductances calculated using the formulas of Robinson et al. (1987) are inconsistent with simple applications of Ohm's law. At δB_Z extrema $J_\parallel = I_P = \sum_P E_Y$, independent of conductivity profiles. Here, $\sum_P$ represents the local value of the Pedersen conductance at the transition between upward and downward FACs. In these regions the formulas of Robinson et al. (1987) predict $\sum_P$ values of a few mhos. For the cases shown in Figs. 5a and c, $J_\parallel \approx 1.2$ A/m. F13 and F15 measured E_Y values of 91.5 and 42.5 mV/m (Table 1), respectively. Corresponding $\sum_P$ values of 13.1 and 28.2 mho exceed those shown in Fig. 5 between the upward and downward current sheets. Thus, $\sum_P$ gradients alone cannot account for the difference between the two methods of estimation.

2. Limits of applicability: At large solar-zenith angles Robinson's formulas estimate $\sum_P$ and $\sum_H$ for a given energy flux and average energy of precipitating electrons. Robinson et al. (1987) explicitly exclude contributions of precipitating electrons with energies <500 eV and all protons to conductances, and explicitly caution against use of their formulas when the energies of electrons are low.

During the April 2000 storm, neglect of this limiting condition leads to underestimates of $\sum_P$. Data in Fig. 3 indicate that E_{AVE} <500 eV. Electrons with these energies are stopped through collisions with thermospheric neutrals at altitudes above 190 km (Rees, 1964). Ionization created by these incident electrons places the Pedersen current-closure layer at F layer altitudes. Few electrons had sufficient energy to create E-region ionization (Fig. 4c). In the evening sector, precipitating ions carried the downward FAC (Fig. 4d). Galand and Richmond (2001) and Galand et al. (2001) showed that precipitating protons affect ionospheric conductances. At this point the dependence of $\sum_P$ on precipitating ions/electron fluxes is not sufficiently understood, and limits our ability to estimate "Joule heat" dissipation.

Uncritical applications of the Robinson formulas, irrespective of location on the globe, can also lead to significant errors. Assume that at δB_Z extrema, the SSJ4 sensors on F13 and F15 had measured the same values of Φ_E and E_{AVE}. The Robinson formulas predict the same $\sum_P$ and $\sum_H$ beneath the two satellites. This cannot be correct. The Pedersen conductivity is given by $\sum_P \approx (ne/B)\cdot(\nu_{in}/\omega_i)$, where n, ν_{in}, and ω_i represent the plasma density, the ion-neutral collision frequency, and the ion gyrofrequency, respectively. To a first approximation, electrons precipitating at the locations of F13 and F15 would produce the same plasma density profiles. Assuming similar thermospheric profiles, the ν_{in} height profiles should also be similar. However, since σ_P is proportional to B^{-2} in the Pedersen current layer, values of $\sum_P = \int \sigma_P \, ds$ should be quite different. The magnetic field measured by F13 was 1.58 times that observed by F15. Thus, for the same particle inputs, $\sum_P$ at the location of F13 should be ~40% of that at the location of F15. At the interface between the two FACs, we estimated that at the location of F13 $\sum_P$ was 46% of the value at F15.

3. Transmission line effects: Table 3 combines δB_Z and E_Y observed by F13 and F15 in upward and downward FAC sheets (Table 2) with measured values of V_{AS} to calculate $\sum_P/\sum_A$ and R. Columns 5 and 6 of Table 3 show the calculated intensities of electric and magnetic fields for incident Alfvén waves $E_Y^i = E_Y/(1+R)$ and $\delta B_Z^i = \delta B_Z/(1-R)$. Except for the downward FAC crossed by F13, reflection coefficients are near 0.9. In all cases the E_Y^i values are much larger than are typically observed at 840 km. Note that in all cases the ratios of $E_Y/\delta B_Z$ for the incident and reflected waves agree with the local Alfvén speeds derived from measured plasma densities and magnetic fields. Poynting fluxes carried by the incident waves are of order 0.1 W/m^2 = 100 erg/(cm^2 s). As seen below, even though 50–80% of this energy is reflected, the electromagnetic energy absorbed by the ionosphere and thermosphere greatly exceeds the energy deposited by precipitating electrons and ions.

Table 3
Alfvén wave-reflection coefficients

DMSP/$j_\parallel$	$\Delta\delta B_Z/\Delta E_Y$	$\sum_P/\sum_A$	R	E_Y^i (mV/m)	δB_Z^i (nT)
F13 ⇑	$7.40\cdot10^{-6}$	5.5	−0.70	338	435
F13 ⇓	$3.79\cdot10^{-5}$	28.4	−0.93	329	452
F15 ⇑	$3.43\cdot10^{-5}$	18.9	−0.90	369	668
F15 ⇓	$3.91\cdot10^{-5}$	21.5	−0.91	277	509

DMSP electric and magnetic field measurements provide information about the ratio $\sum_P/\sum_A$, but say nothing about the value of either quantity. Calculations summarized in the third column of Table 3 indicate that $\sum_P/\sum_A$ ratios are relatively large. At ionospheric altitudes Alfvén impedances are typically of the order of 1 mho. Thus, $\sum_P$ values are easy to reconcile with estimates in Table 2. On the other hand, if we assume that $\sum_P$ has values determined using the formulas of Robinson et al. (1987), then proportionately lower values of $\sum_{AR}$ are required. This in turn would require that $V_{AR} > V_{AS}$, a conclusion that is difficult to reconcile with plasma density profiles that typically decrease exponentially with altitude in the topside ionosphere.

The fact that SSIES and SSM detect superposed downward and upward propagating Alfvén waves has practical consequences. Measurements of δB_Z and E_Y can be used to estimate the net Poynting fluxes associated with the

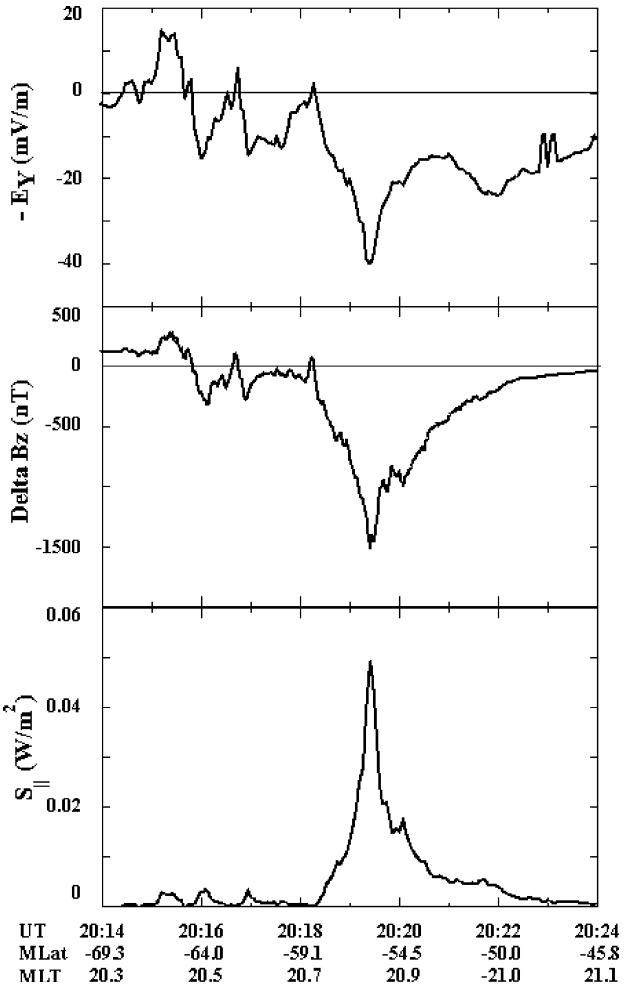

Fig. 6. Estimated net Poynting flux (bottom) in Watts per square meter based on electric (top) and magnetic (middle) perturbations measured by DMSP F15 near 20:20 UT in the southern auroral oval.

current-carrying waves. Eq. (10) indicates that the net Poynting flux is a direct measure of electromagnetic energy dissipated in the ionosphere–thermosphere magnetically conjugate to the spacecraft. As an example we again turn attention to electromagnetic perturbations detected by F15 during the southern auroral pass near 20:20 UT. Fig. 6 shows measured values of $-E_Y$ (top) and δB_Z (middle) as well as the inferred $S_\parallel$ (bottom) plotted as functions of UT MLat and MLT. The maximum net Poynting flux was $\sim$0.05 W/m^2. At the location of F13 it was about twice this value. The integrated electromagnetic energy flowing into the ionosphere across the structure was $\sim$21 kW/m. Measurements from multiple DMSP satellites indicate that the large FAC structures extend for at least an hour in local time. Over a 15° spread in longitude the total power input to the ionosphere exceeds 21 GW. If we assume that the FAC systems detected by DMSP satellites occurred in both hemispheres and extended for $\sim$3 h in local time in both the evening and morning sectors, their total rate of energy in put is 252 GW. For comparison, the two closest-in-time estimates of HPI were 30.1 and 25.9 GW. The input to the ionosphere in 20 min would be $\sim$300 TJ. This represents $\sim$5% of the total kinetic energy of the ring current particles estimated using the Dessler–Parker–Sckopke relation with Dst = −250 nT (Carovillano and Maguire, 1968).

5. Discussion and conclusions

Our analysis of particle and field data acquired by DMSP satellites during the main phase of the April 6, 2000 magnetic storm uncovered several under-appreciated facets of space-weather modeling. We have focused on nearly simultaneous observations of intense ($J_\parallel > 1$ A/m) FACs in the evening and dawn MLT sectors. Large magnetic perturbations, at the transition between the R1 and R2 currents occurred between at relatively low magnetic latitudes between the B_{2e} and B_{2i} auroral boundaries (Newell et al., 1996). Near the R1/R2 interface ionospheric conductances estimated from simultaneous electric and magnetic field variations were systematically larger than those determined from electron fluxes (Robinson et al., 1987). While we understand that the energy of current-carrying electrons was outside the model's range of applicability, still questions remain. Why were plasma sheet electrons in such high numbers and low energies near the maximum epoch of so intense a magnetic storm?

The fact that ground stations detected no commensurate magnetic perturbations while DMSP was detecting intense FACs is both intelligible and worrisome. Kamide et al. (1981) and Raeder et al. (2001) have already cautioned that integration of space data into AMIE simulations of superstorms must be exercised with great care lest they produce misleading results. DMSP observations presented here are unusual, but not unique. An informal survey of our DMSP database shows that $J_\parallel > 1$ A/m events regularly occur during the main phases of magnetic storms with Dst <-200 nT. Distinct ground signatures accompanied many, but not all, of the intense stormtime FAC events. At the suggestion of G. Lu, (private communication, 2002) we examined DMSP particle and field data acquired during the superstorms of July 15, 2000 and March 31, 2001. DMSP measurements during both storms bore striking similarities to the observations reported here. Again, intense FACs observed at 840 km were unmatched by strong magnetic perturbations at the ground. In both of these superstorms the intense FACs were observed at latitudes well equatorward of the normal auroral oval, and $E_{AVE} \leqslant 500$ eV for precipitating electrons.

Merely pointing out that the reliability of space-environment specifications deteriorates under certain stressed conditions is of limited usefulness. In the present case, uncritical reliance on ground magnetometer and/or energetic particle measurements to estimate auroral electrodynamics and $\sum_P$ can be misleading. Consequent errors lead to serious underestimates of the electromagnetic energy input to the ionosphere. This has broad, practical consequences for understanding the space-weather of magnetospheric plasma transport and thermospheric heat budgets. This in turn has practical consequences for predicting orbital trajectories of space debris and thus the correct collision-avoidance procedures needed to protect space assets.

In modeling magnetospheric plasma transport it is useful to close the fluid equations by assuming a physics-based relationship between the plasma's pressure P and density n. A polytropic relationship in the form $P/n^\gamma = \text{constant}$ is convenient. Adiabatic transport with $\gamma = 5/3$, assumes that during transport the plasma neither gains nor loses heat. Borovsky et al. (1998) empirically demonstrated that systematic departures from adiabatic transport occur at radial distances between 15 and 6.6 R_E where γ decreases from 1.67 to $\sim$1.5. After comparing several possible mechanisms, they conclude that auroral ion precipitation accounts for a large fraction of the entropy loss. Relatively weak HPI contributions to energy loss suggest a reassessment of EM disbursements.

Electromagnetic fields can only interact directly with plasma constituents of the upper atmosphere. Through collisions and chemical interactions with neutrals, electrons and ions transfer supplemented energy to the thermosphere. Some thermospheric energy radiates away. However, a significant fraction is transferred to the directed (winds) and random (thermal) motion of neutrals. Main-phase generated winds in the thermosphere (Scherliess and Fejer, 1997) are thought to be responsible for the suppression of equatorial plasma bubble activity during the recovery phase of magnetic storms (Huang et al., 2001). Thermal energy transferred to the neutrals increases thermospheric scale heights and thereby the drag that the atmospheric exert on space objects. Thermal uplift of molecular species alters ion chemical reaction rates reducing F-layer plasma densities.

Raeder et al. (2001) correctly pointed to knowledge of conductance distributions as critical for realistic space-

weather modeling. Our intention in pointing out real, if understandable, failures of conductance models is to raise awareness about a lurking problem and suggest practical ways around it. By taking advantage of the transmission-line properties of the auroral circuit it is possible to calculate electromagnetic energy inputs to the ionosphere without having to make any assumption about the conductance. Eq. (13) shows that Poynting vectors constructed from measured electric- (E_Y) and magnetic- (δB_Z) field perturbations are equivalent to the energy fluxed of superposed incident and reflected Alfvén waves that carry field-aligned current. With knowledge of locally measured magnetic fields and plasma's mass densities, we can calculate the wave-reflection coefficients [Eq. (11)]. Fig. 6 shows a practical example of the calculated $S_{\parallel}$ equivalent to the rate at which EM energy is transferred to and dissipates in the ionosphere. With careful attention to SSIES and SSM measurements this example is transferable to the analysis of data from DMSP satellites that carry both sensors.

Our key result is the demonstration of a new technique for quantifying the rate at which EM energy is transferred to the ionosphere using in situ electric and magnetic field measurements alone. While perhaps useful, explicit knowledge of the conductances beneath the spacecraft is unnecessary. Application of the technique provides modelers with empirical boundary conditions for calculating how the energy dissipates/partitions in the ionosphere–thermosphere system. In no way do we propose that DMSP Poynting-vector measurements supplant other methods for estimating global energy inputs. The sparse spatial/temporal coverage provided by polar-orbiting satellites alone, would render the suggestion impractical. Rather, satellite systems such as DMSP and Iridium offer complementary information for assimilation into AMIE and/or other space-weather models to improve environment specifications and forecasts.

Acknowledgements

Research presented in this report was supported by the Air Force Office of Scientific Research Task 2311SDA3. The authors are especially grateful to L. C. Gentile for editorial assistance and to the Kyoto World Geomagnetic Data Center [http://swdcdb.kugi.kyoto-u.ac.jp/index.html] for providing comprehensive geomagnetic indices. Interplanetary environment data was obtained from the ACE web site [http://www.srl.caltech.edu/ACE/].

References

Borovsky, J.E., Thomsen, M.F., Elphic, R.C., Cayton, T.E., McComas, D.J. The transport of plasma sheet material from the distant tail to geosynchronous orbit. J. Geophys. Res. 103, 20,297–20,331, 1998.

Brekke, A., Kamide, Y. On the relationship between Joule and frictional heating in the polar ionosphere. J. Atmos. Terr. Phys. 58, 139–144, 1996.

Burke, W.J., Machuzak, J.S., Maynard, N.C., Basinska, E.M., Erickson, G.M., Hoffman, R.A., Slavin, J.A., Hanson, W.B. Auroral ionospheric signatures of the plasma sheet boundary layer in the evening sector. J. Geophys. Res. 99, 2489–2500, 1994.

Carovillano, R.L., Maguire, J.J. Magnetic energy relationships in the magnetosphere. In: Carovillano, R.L., McClay, J.F., Radoski, H.R., Reidel, D. (Eds.), Physics of the Magnetosphere. Dordrecht, Holland, pp. 290–300, 1968.

Dessler, A.J. The evolution of arguments regarding the existence of field-aligned currents, in: Potemra, T.A. (Ed.), Magnetospheric Currents, American Geophysical Union, Monograph 28, Washington, DC, pp. 22–28, 1984.

Egeland, A., Kristin Birkeland. The man and the scientist, in: Potemra, T.A. (Ed.), in Magnetospheric Currents, American Geophysical Union, Monograph 28, Washington, DC, pp. 1–16, 1984.

Evans, D.S. Global statistical patterns of auroral phenomena, in: Proceedings of Symposium on Quantitative Modeling of Magneto-spheric-Ionospheric Coupling Processes, Kyoto, pp. 325–340, 1987.

Fukushima, N. Generalized theorem for no ground magnetic effect of vertical currents connected with Pedersen currents in the uniform conducting ionosphere. Rep. Ionos. Space Res. Jpn. 30, 35–40, 1976.

Fung, S.F., Hoffman, R.A. Finite geometry effects of field-aligned currents. J. Geophys. Res. 97, 8569–8579, 1992.

Galand, M., Fuller-Rowell, T.J., Codrescu, M.V. Response of the upper atmosphere to auroral protons. J. Geophys. Res. 106, 127–140, 2001.

Galand, M., Richmond, A.D. Ionospheric electrical conductances produced by auroral proton precipitation. J. Geophys. Res. 106, 117–126, 2001.

Gary, J.B., Heelis, R.A., Hanson, W.B., Slavin, J.A. Field-aligned Poynting flux observations in the high-latitude ionosphere. J. Geophys. Res. 99, 11,417–11,428, 1994.

Gussenhoven, M.A., Hardy, D.A., Heinemann, N. Systematics of the equatorward diffuse auroral boundary. J. Geophys. Res. 88, 5692–5708, 1983.

Hardy, D.A., Schmidt, L.K., Gussenhoven, M. S., Marshall, F.J., Yeh, H.C., Shumaker, T.L., Huber, A., Pantazis, J. Precipitating electron and ion detectors (SSJ/4) for block 5D/Flights 4–10 DMSP satellites: calibration and data presentation, Tech. Rep., *AFGL-TR-84-0317*, Air Force Geophys. Lab., Hanscom Air Force Base, Mass, 1984.

Huang, C.Y., Burke, W.J. Transient sheets of field-aligned current observed by DMSP during the main phase of a superstorm. J. Geophys. Res. 109, A06303, doi:10.1029/2003JA010067, 2004.

Huang, C.Y., Burke, W.J., Machuzak, J.S., Gentile, L.C., Sultan, P.J. DMSP observations of equatorial plasma bubbles in the topside ionosphere near solar maximum. J. Geophys. Res. 106, 8131–8142, 2001.

Iijima, T., Potemra, T.A. Field-aligned currents in the dayside cusp observed by TRIAD. J. Geophys. Res. 81, 5971–5979, 1976.

Iijima, T., Potemra, T.A. Large-scale characteristics of field-aligned currents associated with substorms. J. Geophys. Res. 83, 599–615, 1978.

Jackson, J.D. Classical Electrodynamics. John Wiley & Sons, New York, 1962.

Kamide, Y., Richmond, A.D., Matsushita, S. Estimation of ionospheric electric fields, ionospheric currents, and field-aligned currents from ground magnetic records. J. Geophys. Res. 86, 801–813, 1981.

Kan, J.R., Sun, W. Simulation of the westward traveling surge and Pi2 pulsations during substorms. J. Geophys. Res. 90, 10911–10922, 1985.

Kelley, M.C., Knudsen, D.J., Vickrey, J.F. Poynting flux measurements on a satellite: a diagnostic tool for space research. J. Geophys. Res. 96, 201–208, 1991.

Knipp, D.J., Tobiska, W.K., Emery, B.A. Direct and indirect thermospheric heating sources for solar cycle 21–23. Sol. Phys. 224 (1–2), 495–505, 2004.

Lyons, L.R. Field-aligned currents versus electric potential relation and auroral electrodynamics, in: Akasofu, S.-I., Kan, J.R. (Eds.), Physics of Auroral Arc Formation, Geophysics Monograph 25, AGU, Washington, DC, pp. 252–269, 1981.

Newell, P.T., Feldstein, Y.I., Galperin, Y.I., Meng, C.-I. Morphology of nightside precipitation. J. Geophys. Res. 101, 10,737–10,748, 1996.

Nishida, A. Coherence of geomagnetic DP 2 fluctuations with interplanetary magnetic variations. J. Geophys. Res. 73, 5549–5560, 1968.

Ober, D.M., Maynard, N.C., Burke, W.J. Testing the Hill model of transpolar saturation. J. Geophys. Res. 108 (A12), 1467, doi:10.1029/2003JA010154, 2003.

Raeder, J., McPherron, R.L., Frank, L.A., Kokubun, S., Lu, G., Mukai, T., Peterson, W.R., Sigwarth, J.B., Singer, H.J., Slavin, J.A. Global simulation of the geospace environment modeling substorm challenge event. J. Geophys. Res. 106, 381–396, 2001.

Rees, M.H. Note on the penetration of electrons into the Earth's atmosphere. Planet. Space Sci. 12, 722–725, 1964.

Rich, F.J., Hairston, M. Large-scale convection patterns observed by DMSP. J. Geophys. Res. 99, 3827–3844, 1994.

Richmond, A.D. Assimilatative mapping of ionospheric electrodynamics. Adv. Space Res. 6 (1), 59–63, 1992.

Richmond, A.D., Kamide, Y. Mapping electrodynamic features of the high-latitude ionosphere from localized observations: technique. J. Geophys. Res. 93, 5741–5759, 1988.

Robinson, R.M., Vondrak, R.R., Miller, K., Dabbs, T., Hardy, D. On calculating ionospheric conductances from the flux and energy of precipitating electrons. J. Geophys. Res. 92, 2565–2570, 1987.

Romer, R.H. Alternatives to the Poynting vector. Amer. J. Phys. 50, 1166–1168, 1982.

Scherliess, L., Fejer, B.G. Storm time dependence of equatorial disturbance dynamo zonal electric fields. J. Geophys. Res. 102, 24,037–24,046, 1997.

Siscoe, G.L., Erickson, G.M., Sonnerup, B.U.Ö., Maynard, N.C., Schoendorf, J.A., Siebert, K.D., Weimer, D.R., White, W.W., Wilson, G.R. Hill model of trans-polar saturation: comparison with MHD simulation. J. Geophys. Res. 107 (A6), 1075, doi:10.1029/2001JA000109, 2002.

Song, P., Vasyliunas, V.M., Ma, L. A three-fluid model of solar wind-magnetosphere–ionosphere–thermosphere coupling. In: Lui, A.T.Y., Kamide, Y., Consolini, G. (Eds.), Multi-Scale Coupling of Sun-Earth Processes, Elsevier B.V., pp. 446–447, 2005.

Sonnerup, B.U.Ö. Magnetopause reconnection rate. J. Geophys. Res. 79, 1546–1549, 1974.

Thayer, J.P., Vickrey, J.F. On the contribution of the thermospheric neutral wind to high latitude energetics. Geophys. Res. Lett. 19, 265–268, 1992.

Thayer, J.P., Vickrey, J.F., Heelis, R.A., Gary, J.B. Interpretation and modeling of the high-latitude electromagnetic energy flux. J. Geophys. Res. 100, 19,715–19,728, 1995.

Vasyliunas, V.M., Song, P. Meaning of ionospheric Joule heat. J. Geophys. Res. 110 (A0230), doi:10.1029/JA2004JA010615, 2005.

Wallis, D.D., Budzinski, E.E. Empirical models of height integrated conductivities. J. Geophys. Res. 86, 125–138, 1981.

Waters, C.L., Anderson, B.J., Greenwald, R.A., Barnes, R.J., Ruohoniemi, J.M. High-latitude Poynting Flux from combined Iridium and SuperDARN data. Annal. Geophys. 22, 2861–2875, 2004.

Winningham, J.D., Heikkila, W.J. Polar cap auroral electron fluxes observed with Isis 1. J. Geophys. Res. 79, 949–958, 1974.

Winningham, J.D., Yasuhara, F., Akasofu, S.-I., Heikkila, W.J. The latitudinal morphology of 10-eV to 10-keV electron fluxes during magnetically quiet and disturbed times in the 2100–0300 MLT sector. J. Geophys. Res. 80, 3148–3171, 1975.

Zhu, L., Sojka, J.J., Schunk, R.W., Crain, D.J. Influence of horizontal inhomogeneity in the ionosphere on the reflection of Alfvén waves. Geophys. Res. Lett. 20, 313–316, 1993.